Author/s:
Chen, J;Spoljaric, S;Calatayud-Sanchez, A;Alvarez-Braña, Y;Caruso, F

Title:
Engineering Metal-Phenolic Network Nanoparticles via Microfluidics

Date:
2023-10-18

Citation:
Chen, J., Spoljaric, S., Calatayud-Sanchez, A., Alvarez-Braña, Y. & Caruso, F. (2023). Engineering Metal-Phenolic Network Nanoparticles via Microfluidics. ACS Applied Materials and Interfaces, 15 (41), pp.48050-48059. https://doi.org/10.1021/acsami.3c11889.

Engineering Metal–Phenolic Network Nanoparticles via Microfluidics

*Jingqu Chen,[1‡] Steve Spoljaric,[1‡] Alba Calatayud-Sanchez,[1,2,3] Yara Alvarez-Braña,[1,2,3] and Frank Caruso[1]**

[1]Department of Chemical Engineering, The University of Melbourne, Parkville, Victoria 3010, Australia

[2]Microfluidics Cluster UPV/EHU, Analytical Microsystems & Materials for Lab-on-a-Chip (AMMa-LOAC) Group, Analytical Chemistry Department, University of the Basque Country UPV/EHU, Leioa, Spain

[3]Microfluidics Cluster UPV/EHU, BIOMICs microfluidics Group, Lascaray Research Center, University of the Basque Country UPV/EHU, Vitoria-Gasteiz, Spain

*Corresponding author. E-mail: fcaruso@unimelb.edu.au

[‡]These authors contributed equally to this work.

KEYWORDS Microfluidics, Nanoparticles, Polyphenols, Metal–organic materials, Bioactive materials

ABSTRACT

Microfluidics opens new avenues for materials engineering as it enables scalable synthesis and provides highly controllable environments for reactions. Herein, we seek to leverage

microfluidics to engineer the properties of (bioactive) metal–phenolic network nanoparticles (MPN NPs), an emerging and highly modular nanoparticle platform for the incorporation and delivery of bioactive cargo. By varying the microfluidics operating (flow rate ratio, total flow rate, temperature) and NP composition, we assemble MPN NPs, which consist of poly(ethylene) glycol, biomacromolecules, metal ions, and polyphenols. Compared to MPN NPs prepared via bulk assembly, the microfluidics-assembled MPN NPs possess a broader tunable size range (i.e., ~40–330 nm versus ~45–220 nm for bulk-assembled NPs) and a higher (by ~30%) protein loading. While bulk-assembled MPN NPs show pH-responsive protein release (e.g., ~50% at pH 7; ~25% at pH 9; 48 h), the MPN NPs prepared via microfluidics at a flow rate ratio of 1:1 display pH and slight thermal-responsive protein release behaviors. For instance, higher release efficiencies can be obtained by increasing the temperature from 4 to 20 ℃ when using a flow rate ratio of 1:1. Furthermore, assembly at a 1:1 flow rate ratio overall enables greater tunability of protein release profiles than at higher flow rate ratios. While bulk-assembled NPs display a higher degree of cell association, NPs assembled via both strategies can be internalized by cells after 24 h. These findings provide new insights into engineering properties of metal–organic materials via microfluidics, which is expected to advance their development and application.

INTRODUCTION

Engineering functional materials with tunable properties is a growing endeavor in both fundamental and applied research owing to the widespread application of such materials in a range of areas. There are diverse pathways for engineering functional materials, including mechanical stirring/vortexing,[1–3] phase separation,[4,5] spray assembly,[6–8] ultrasonication,[9–11] and microfluidics.[12–18] Among these strategies, microfluidics-mediated materials engineering has received significant attention owing to: i) its ability to synthesize materials reproducibly and at scale, as required for pilot studies and commercialization;[19] ii) the large surface area and

efficient mass and heat transfer that the fluids in the microchannels provide, thereby allowing efficient mixing and reactions of reagents;[20] and iii) the highly controllable environment (via generating laminar flow) for bio(chemical) reactions, thus enabling more precise manipulation of material structure and properties.[21,22]

Recently, we reported a bioactive metal–phenolic network nanoparticle (b-MPN NP) platform that can incorporate a wide range of active biomacromolecules. The broad functionality of the platform was also demonstrated in gene silencing, RNA degradation, cell apoptosis, and catalysis.[23] The b-MPN NPs can be prepared from a diverse library of building blocks and typically in bulk via the sequential addition of aqueous solutions of poly(ethylene) glycol (PEG), biomacromolecules, metal ions, and polyphenols into a glass vessel, followed by stirring (i.e., for homogenization of NPs).[23] During the NP assembly, PEG acted as a seeding agent to increase the local concentration of biomacromolecules, metal ions, and polyphenols, while the formation of NP was initiated upon the addition of polyphenols and predominantly mediated through hydrophobic interactions and coordination.[23] The flow regime generated in this bulk assembly is primarily turbulent due to vigorous agitation.[24] In contrast, microfluidics can generate a defined laminar flow, which can provide mixing conditions and reaction interfaces that are distinct from those present in bulk assembly.[22] Therefore, engineering MPN NPs, including b-MPN NPs, via microfluidics, combined with the modular nature (i.e., in terms of the choice of building blocks) of metal–phenolic materials,[23,25] may provide a viable pathway to expand and/or alter their property profiles and provide new insights into the structure–property relationships of MPN NPs.

In the present study, MPN NPs without and with bioactive cargo—i.e., proteins (e.g., bovine serum albumin (BSA), pepsin (PEP), glucose oxidase (GOx), and lysozyme (LYZ))—are assembled using a NanoAssemblr Ignite microfluidic system (Figure 1). The influence of operating parameters (i.e., flow rate ratio, total flow rate, and temperature) and NP composition

parameters (i.e., Fe^{III} concentration, PEG molecular weight (M_w), protein type) on the size and morphology, physicochemical properties, and cellular interactions of the NPs are systemically evaluated. Compared with the bulk-assembled b-MPN NPs, the microfluidics-assembled b-MPN NPs are larger and display a higher (by ~30%) protein loading, likely owing to the predominant laminar flow produced by microfluidics, which enables fine mixing between the precursors with a defined concentration distribution alongside the microchannels.[22] The bulk-assembled b-MPN NPs and b-MPN NPs assembled via microfluidics using a flow rate ratio of 1:1 display a similar pH-responsive protein release profile, with ~60% release observed at pH 7 after 48 h. However, the release profile of the microfluidics-assembled NPs can also be tuned by altering the temperature (e.g., slower release pattern at 4 °C compared to 20 and 37 °C) and flow rate ratio (e.g., NPs prepared at flow rate ratios of 3:1 and 10:1 overall showed <10% protein release regardless of pH and temperature). The bulk-assembled b-MPN NPs show a higher degree of cell association compared with the microfluidics-assembled b-MPN NPs; while the NPs prepared via both assembly strategies can be internalized by cells after incubation for 24 h. The present study demonstrates the use of microfluidics in synthesizing b-MPN NPs with tunable physicochemical and nano–bio properties; the findings are expected to facilitate the future development and application of these b-MPN NPs.

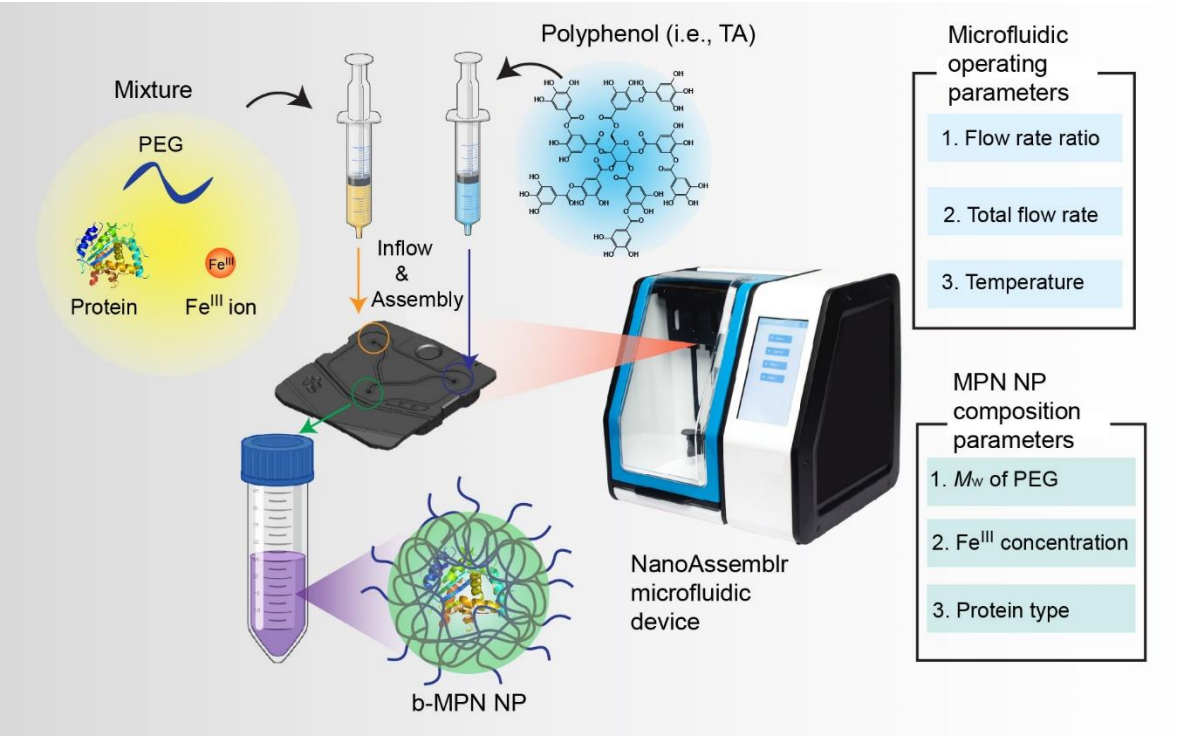

Figure 1. Schematic of the preparation of b-MPN NPs using the NanoAssemblr microfluidic device.

EXPERIMENTAL SECTION

Materials. PEG (M_w: 1.1, 2, 5, 10, and 35 kDa), tannic acid (TA), iron(III) chloride hexahydrate ($FeCl_3 \cdot 6H_2O$), BSA, PEP, GOx, LYZ, (3-(N-morpholino)propanesulfonic acid) (MOPS), and sodium acetate (NaOAc) were purchased from Sigma-Aldrich and used as received. Dulbecco's phosphate-buffered saline (DPBS), phenazine methosulfate (PMS), Dulbecco's modified Eagle's medium (DMEM), and 2,3-bis[2methoxy-4-nitro-5-sulfophenyl]-2*H*-tetrazolium-5-carboxyanilide inner salt (XTT) were obtained from Life Technologies. Milli-Q water with a resistivity greater than 18.2 MΩ cm^{-1} was obtained from a Milli-Q Synergy purification system (Merck, USA). All aqueous solutions were filtered with 220 nm diameter membranes before cell association experiments.

Preparation of b-MPN NPs via Microfluidics. b-MPN NPs were prepared using a NanoAssemblr Ignite microfluidic device (Precision NanoSystems Inc., Vancouver, BC, Canada), which was equipped with a Y-shape NxGen micromixer cartridge featuring circular

structures within the flow route for increased mixing efficiency (Figure 1, Figure S1). The b-MPN NPs were composed of PEG, TA, $FeCl_3 \cdot 6H_2O$ (Fe^{III}), and either LYZ, BSA, PEP, or GOx. In a typical preparation, individual stock solutions of PEG (20 mg mL^{-1}), TA (1.3 mg mL^{-1}), $FeCl_3 \cdot 6H_2O$ (0, 0.5, 2.5, 5, 12.5, or 25 mg mL^{-1}), and BSA, PEP, GOx, or LYZ (10 mg mL^{-1}) in Milli-Q water were first prepared. A mixture consisting of PEG, protein, and Fe^{III} stock solutions was then prepared at a weight ratio of 4:1:0.32 (PEG:protein:Fe^{III}). The mixture and the TA stock solution were separately loaded into 3 mL polypropylene syringes and then simultaneously injected into the device via the center and right injection ports, respectively. Figure S2 shows the detailed steps in preparing b-MPN NPs via microfluidics. The NanoAssemblr Ignite operates by only allowing simultaneous injection of both ports, however the design of the device and cartridge allow the mixture and TA solutions to be placed in either the center or right injection ports. Following fabrication, the b-MPN NPs were washed twice via centrifugation (8000 *g*, 10 min) and redispersed in an alkaline buffer solution (2 mM MOPS, pH 7) for better stability.

Unless otherwise stated, all b-MPN NPs were fabricated using a TA:mixture flow rate ratio of 1:1, a total flow rate of 10 mL min^{-1}, a temperature of 24 °C, an Fe^{III} concentration of 5 mg mL^{-1}, and a PEG M_w of 2 kDa.

Preparation of b-MPN NPs via Bulk Assembly. Bulk-assembled b-MPN NPs were prepared according to our recent report.[23] Briefly, PEG (2 kDa), proteins, Fe^{III}, and TA were sequentially added to a glass vial containing 2 mL of water followed by stirring. The amounts of PEG, proteins, Fe^{III}, and TA added were the same as for microfluidic assembly using a 1:1 flow rate ratio. Following assembly, the b-MPN NPs were washed twice via centrifugation (8000 *g*, 10 min) and redispersed in an alkaline buffer solution (2 mM MOPS, pH 7) for better stability.

Characterization of b-MPN NPs. The zeta (ζ)-potential, number mean size distribution, and polydispersity index (PDI) of the NPs were measured in 2 mM MOPS (pH 7) on a Zetasizer Nano-ZS instrument (Malvern Instrument, UK). The concentration of NPs (i.e., number of NPs mL^{-1}) was determined using a NanoSight N300. The morphologies of the NPs were analyzed by transmission electron microscopy (TEM) using an FEI Tecnai TF20 instrument with an operation voltage of 80 kV. UV–vis absorption spectra were recorded on a SPECORD 250 Plus UV–vis spectrophotometer.

Quantification of Protein Loading and Cumulative Release. The loading and release of BSA from b-MPN NPs were quantified by a modified Bicinchoninic acid (BCA) assay. First, BSA-MPN NPs were prepared via bulk assembly and microfluidics (using TA-to-mixture flow rate ratios of 1:1, 3:1, and 10:1). The resultant NPs were centrifuged (8000 *g*, 10 min), and the supernatant of each type of NPs after the first centrifugation was collected for quantifying BSA loading. To investigate the effect of pH on BSA release, the BSA-MPN NPs were dispersed in different buffer solutions (2 mM; NaOAc pH 4, MOPS pH 7, MOPS pH 9) and centrifuged after 1, 5, 15, 24, and 48 h. After each centrifugation step, the supernatant (500 μL) was collected from each sample, and the same buffer solution (500 μL) was added to the NP suspensions. To investigate the effect of temperature on BSA release, the BSA-MPN NPs were dispersed in 2 mM MOPS (pH 7) and incubated at 4, 20, and 37 °C. The supernatant was then collected in the same way. The collected supernatant was incubated with BCA reagent in a 1:1 volume ratio and transferred to a 96-well plate (transparent, flat bottom). The absorbance was screened on an Infinite M200 microplate reader (Tecan, Switzerland) with a measurement wavelength of 562 nm. As both polyphenols and environmental pH influence BCA readout, BSA calibration curves of BSA-MPN NPs obtained from each formulation were prepared in water (for quantification of loading) and corresponding buffer solutions (pH 4, 7, 9, for quantification of release) in the presence of PEG, BSA, Fe^{III}, and TA (Figures S3–S5). The

mass ratio of the precursors was 4:1:0.32:1 (PEG:BSA:Fe^{III}:TA for bulk assembly) or according to the flow rate ratio (TA:mixture) set up on the NanoAssemblr Ignite. TA calibration curve could also be obtained via this method to estimate the loading of TA in BSA-MPN NPs. All experiments were performed in triplicates, and data are presented as the mean ± standard deviation (SD).

Protein Release Study via Sodium Dodecyl Sulfate Polyacrylamide Gel Electrophoresis (SDS-PAGE). BSA released after 48 h (pH 7) from the bulk-assembled BSA-MPN NPs and microfluidics-assembled BSA-MPN NPs (using 1:1 flow rate ratio) were collected as per the protocol described in *Quantification of Protein Loading and Cumulative Release*. Aliquots of the released BSA (15 µL), free BSA (15 µL), and TA (15 µL) were mixed with NuPAGE LDS sample buffer (5 µL, 4×), and an aliquot (20 µL) of the mixed sample was loaded into the gel lanes. The gel was run using 1× tris/glycine/SDS running buffer at 100 V until the dye front reached the reference line. Then, the gels were stained with SimplyBlue SafeStain for 1 h under mild shaking and washed with Milli-Q water overnight under mild shaking to visualize protein staining. The stain-free gel was then imaged using Gel Doc (BIO-RAD).

Cell Culture. The human breast adenocarcinoma cell line (MDA-MB-231) was purchased from the American Type Culture Collection. Cells were cultured in complete DMEM supplied with 10 % fetal bovine serum (FBS) at 37 °C, 5 % CO_2, and 95% humidity.

XTT Cell Viability Assay. To evaluate the cytotoxicity of the BSA-MPN NPs assembled via microfluidics and bulk assembly, MDA-MB-231 cells were seeded in a 96-well plate (Costar, Corning) at a density of 8000 cells per well in DMEM supplied with 10% FBS (100 µL) for 20 h. The cell media was then aspirated and replaced with either fresh media (100 µL) (for untreated cells) or the media containing different BSA-MPN NPs at a particle-to-cell ratio ranging from 2×10^5:1 to 4×10^6:1 and further incubated for up to 48 h. After the incubation, the media was replaced with fresh media containing activated XTT (9 mL of 0.2 mg mL^{-1} XTT

in complete DMEM could be activated by adding 22.5 μL of 0.6 mg mL^{-1} PMS in DPBS), and cells were further incubated for 3 h at 37 °C. Finally, cells were screened (via absorbance reading measurements) on an Infinite M200 microplate reader using a measurement wavelength of 475 nm and a reference wavelength of 675 nm. Cell viability was expressed as a percentage by normalizing absorbance to untreated cells. All experiments were performed in quadruplicates, and data are presented as the mean ± SD.

Cell Association Assay via Flow Cytometry. MDA-MB-231 cells were seeded in a 24-well plate (Costar, Corning) at a density of 5×10^4 cells per well in DMEM supplied with 10% FBS (500 μL) for 20 h. b-MPN NPs containing fluorescein isothiocyanate (FITC)-labeled BSA (i.e., BSA_{FITC}-MPN NPs) that were prepared via bulk assembly and microfluidics using TA:mixture flow rate ratios of 1:1, 3:1, and 10:1 were introduced to the well at a particle-to-cell ratio of 5×10^5:1 and incubated for 4 and 24 h. After the treatment, the media was aspirated, and cells were gently rinsed twice with DPBS to remove unbound NPs. The cells were lifted by trypsin, transferred to a 96-well plate (Costar, U-bottom), and further washed three times with DPBS via centrifugation (350 *g*, 5 min). Finally, cells were fixed by redispersing cell pellets in 4 % paraformaldehyde (PFA), and cell association was analyzed by flow cytometry. All experiments were performed in triplicates, and data are presented as the mean ± SD.

Cell Association Assay via Confocal Laser Scanning Microscopy. MDA-MB-231 cells were seeded in a 24-well plate (Costar, Corning) at a density of 5×10^4 cells per well in DMEM supplied with 10 % FBS (500 μL) for 20 h. BSA_{FITC}-MPN NPs that were prepared via bulk assembly and microfluidics using TA:mixture flow rate ratios of 1:1, 3:1, and 10:1 were introduced to the well at a particle-to-cell ratio of 5×10^5:1 and incubated for 4 and 24 h. Following incubation, the media was aspirated, and cells were gently rinsed twice with DPBS to remove unbound NPs. Cells were then fixed by incubating with 4% PFA for 20 min at room temperature (20 °C) followed by light washing with DPBS. The membrane was stained with

Alexa Fluor 594–wheat germ agglutinin conjugate (AF594-WGA; 5 μg mL^{-1}) for 5 min and the nucleus was stained with Hoechst 33342 (1 μg mL^{-1}) for 10 min. Finally, the cells were live-imaged using a Nikon A1R confocal microscope with a 40× water immersion objective.

Colocalization with Lysosomes. MDA-MB-231 cells were seeded at 4 ×10^4 cells per well in Labtek 8-well chamber slides and incubated overnight. BSA_{FITC}-MPN NPs prepared via bulk assembly or microfluidics using a flow rate ratio of 1:1 were then introduced to cells at a particle-to-cell ratio of 5 × 10^5. After 24 h of incubation, the media were aspirated and the cells were gently washed twice with DPBS and fixed with 4% paraformaldehyde for 20 min. The fixed cells were then gently washed twice with DPBS and permeabilized with 0.1% Triton X-100 in DPBS for 5 min and further washed twice. After permeabilization, cells were incubated with 1% BSA in DPBS to block nonspecific binding and incubated overnight with rat anti-LAMP1 monoclonal antibody (2.5 μg mL^{-1}). Then, the cells were gently washed three times with DPBS and incubated with goat antirat AF647 conjugate antibody (2.0 μg mL^{-1}) for 1 h. Cells were gently washed three times with DPBS and incubated with Hoechst 33342 (1 μg mL^{-1}) for 10 min to stain the nucleus, followed by imaging using a Nikon A1R confocal microscope with a 40× water immersion objective.

Minimum Information Reporting in Bio–Nano Experimental Literature (MIRIBEL). The studies conducted herein, including material characterization, biological characterization, and experimental details, conform to the MIRIBEL reporting standard for bio−nano research, and we include a companion checklist of these components in the Supporting Information.[26]

RESULTS AND DISCUSSION

Influence of Microfluidic Operating Parameters. The effects of flow rate ratio on the morphology, size, PDI, and ζ-potential of BSA-MPN NPs were first investigated. Adjusting the flow rate ratio alters the injection volume of TA and the mixture (PEG, Fe^{III}, protein), thereby changing the ratio of TA to PEG, protein, and Fe^{III} during NP assembly (Table S2). As

shown in Figure 2A, the NP suspension changed from purple to red when increasing the flow rate ratio (TA:mixture), suggesting that the TA–Fe^{III} coordination states of the NPs shifted from bis-dominant to tris-dominant.[27] A TA:mixture flow rate ratio of 1:10 yielded BSA-MPN NPs with a size of 17 ± 4 nm and a relatively broad size distribution (i.e., PDI = 0.65; Table S1). Increasing the flow rate ratio to 1:1 resulted in a steady increase in particle size and improvement in monodispersity (Figures S6 and S7), as deduced from the smaller PDIs obtained (from 0.65 to 0.16; Table S1). Notably, a flow rate ratio of 1:1 is the threshold ratio that allows purification of the NPs via centrifugation (Figure 2B, C). However, increasing the flow rate ratio to 3:1 yielded a significant increase in particle size (i.e., 330 ± 71 nm) and irregularly shaped NPs. Further increases in the flow rate ratio to 5:1 and 10:1 resulted in the size reduction of the NPs to ~105 and 58 nm, respectively, with more uniform and spherical structures (Figure 2B, C, Table S1). Increasing the flow rate from 1:1 to 3:1 likely resulted in the accumulation of TA on the surface, as deduced from the shift in ζ-potential from approximately –40 to –60 mV (Figure S8). However, the observed reduction in particle size with improved dispersity (with overall negative ζ-potential) as the flow rate ratio was increased to 5:1 and 10:1 indicate that additional TA may cap the growth of NPs and restabilize the system.

We then explored the effect of total flow rate and temperature on NP assembly. Reducing the total flow rate from 20 to 5 mL min^{-1} resulted in a particle size reduction of ~42 % (i.e., from ~72 to 42 nm) (Figures S9 and S10, Table S3). Increasing the assembly temperature from 24 to 75 °C led to a 44% increase in size of the purified NPs (Figures S11 and S12, Table S4). This size increase may be attributed to the enlarged hydrophobic domain size in the TA–Fe^{III} clusters obtained after thermal treatment.[28] In contrast, adjusting the assembly temperature or total flow rate had a negligible effect on the ζ-potential of the NPs (Figures S13 and S14).

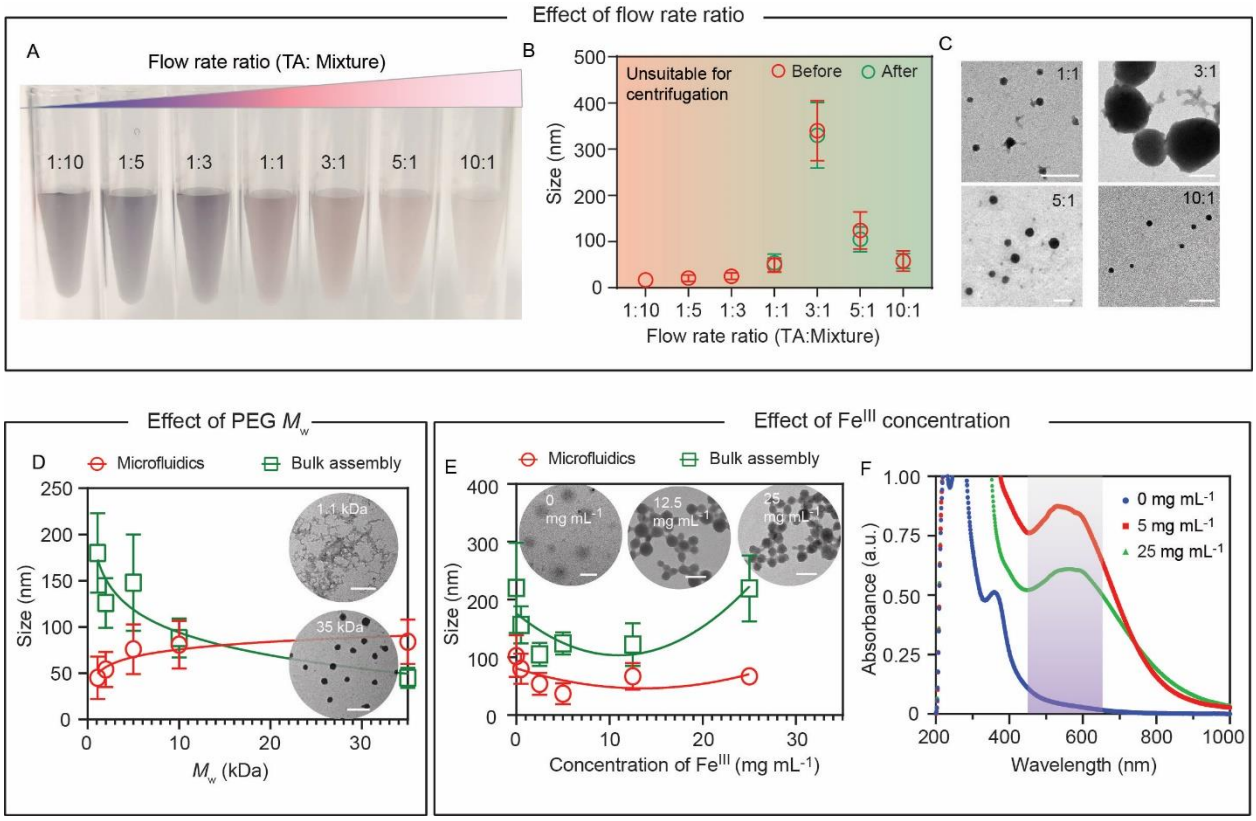

Figure 2. Effect of microfluidics operation and material composition parameters on the properties of BSA-MPN NPs. (A) Digital photograph of BSA-MPN NP suspensions obtained at different flow rate ratios (i.e., TA:mixture). (B) Size of BSA-MPN NPs obtained at different flow rate ratios before and after purification via centrifugation. (C) TEM images of purified BSA-MPN NPs prepared at different flow rate ratios; scale bars are 200 nm. Changes in size of BSA-MPN NPs prepared by microfluidics and bulk assembly as a function of (D) PEG M_w and (E) Fe^{III} concentration. Insets are representative TEM images of the NPs fabricated by microfluidics; scale bars are 100 nm. (F) UV–vis absorption spectra of BSA-MPN NPs prepared by microfluidics as a function of Fe^{III} concentration. The purple region indicates the LMCT band. Three specimens were analyzed for each sample, with data shown as the mean ± SD.

Influence of NP Composition Parameters. The effect of composition parameters, i.e., M_w of PEG and concentration of Fe^{III}, on BSA-MPN NP assembly was then examined. The NPs prepared via microfluidics were compared with those assembled in bulk we reported recently.[23]

For the BSA-MPN NPs prepared via bulk assembly, increasing the M_w of PEG from 1.1 to 35 kDa caused a corresponding reduction (75%) in NP size from ~180 to ~45 nm, which was attributed to an enhanced degree of cross-linking and shielding.[29,30] A reverse trend was observed for the BSA-MPN NPs prepared via microfluidics, where the NP size increased from 45 ± 23 to 84 ± 24 nm as the M_w of PEG increased from 1.1 to 35 kDa (Figure 2D, Figure S15, Table S5) but overall the extent of size change was less significant. The differing size behavior observed in response to varying the M_w of PEG is likely due to the different roles of PEG and mixing conditions. In bulk assembly, all precursors (i.e., PEG, biomacromolecule, Fe^{III}, and TA) are successively added to a glass vial, and PEG serves as a seeding agent to increase the local concentration of the precursors while TA initiates NP assembly through diverse interactions. In contrast, in microfluidics-mediated assembly, PEG is premixed with Fe^{III} and BSA, which may form complexes/agglomerates with comparable sizes that serve as building blocks (Figure S16) and are subsequently interconnected by TA at the junction of the two microfluidic channels to form NPs. The microfluidics-mediated assembly of BSA-MPN NPs using 1.1 kDa PEG might lead to fewer Fe^{III} being complexed and the generation of coordination defects, as indicated by the grey-like color of the NP suspension (Figure S17) and a diminished ligand-to-metal transfer (LMCT) band in the UV–vis absorption spectra (Figure S18A). The reduced amount of complexed Fe^{III} might lead to the formation of small and irregular complexes, resulting in small but highly agglomerated and heterogeneous NPs (PDI = 0.35; Table S5; see inset TEM image in Figure 2D). In contrast, using a higher PEG M_w (e.g., 35 kDa) is likely to form larger and more uniform complexes, thereby producing larger NPs with improved cross-linking density, homogeneity (PDI = 0.07; Table S5), and morphology (see inset TEM image in Figure 2D).

The influence of Fe^{III} concentration on NP assembly was explored, with both microfluidics- and bulk-assembled BSA-MPN NPs displaying the same behavior. For instance, an initial

reduction (from 102 ± 36 to 37 ± 18 nm) in the size of the microfluidics-assembled BSA-MPN NPs occurred with an increase in Fe^{III} concentration from 0 to 5 mg mL^{-1}, followed by a gradual increase in NP size upon further addition of Fe^{III} (Figure 2E, Figure S19, Table S6). Furthermore, the concentration of Fe^{III} influenced the MPN composition in the resultant NPs. For example, when the concentration of Fe^{III} was 0 mg mL^{-1}, the resultant NPs displayed low contrast in the TEM image (Figure 2E inset) and no LMCT band was detected (Figure 2F), likely due to the absence of metal–phenolic coordination. When the Fe^{III} concentration was increased to 5 mg mL^{-1}, a distinct LMCT band was observed, suggesting a bis-dominant coordination state of the MPNs on the NPs.[31,32] Further increasing the concentration to 25 mg mL^{-1} reduced the maximum absorbance at 570 nm from 0.8 to 0.6 (Figure 2F), indicating a reduced proportion of bis-coordination and the redistribution of mono-, bis-, and tris-coordination states in BSA-MPN NPs. No significant trend was noticed in ζ-potential of the NPs upon varying the M_w of PEG or concentration of Fe^{III} (Figures S18B and S20).

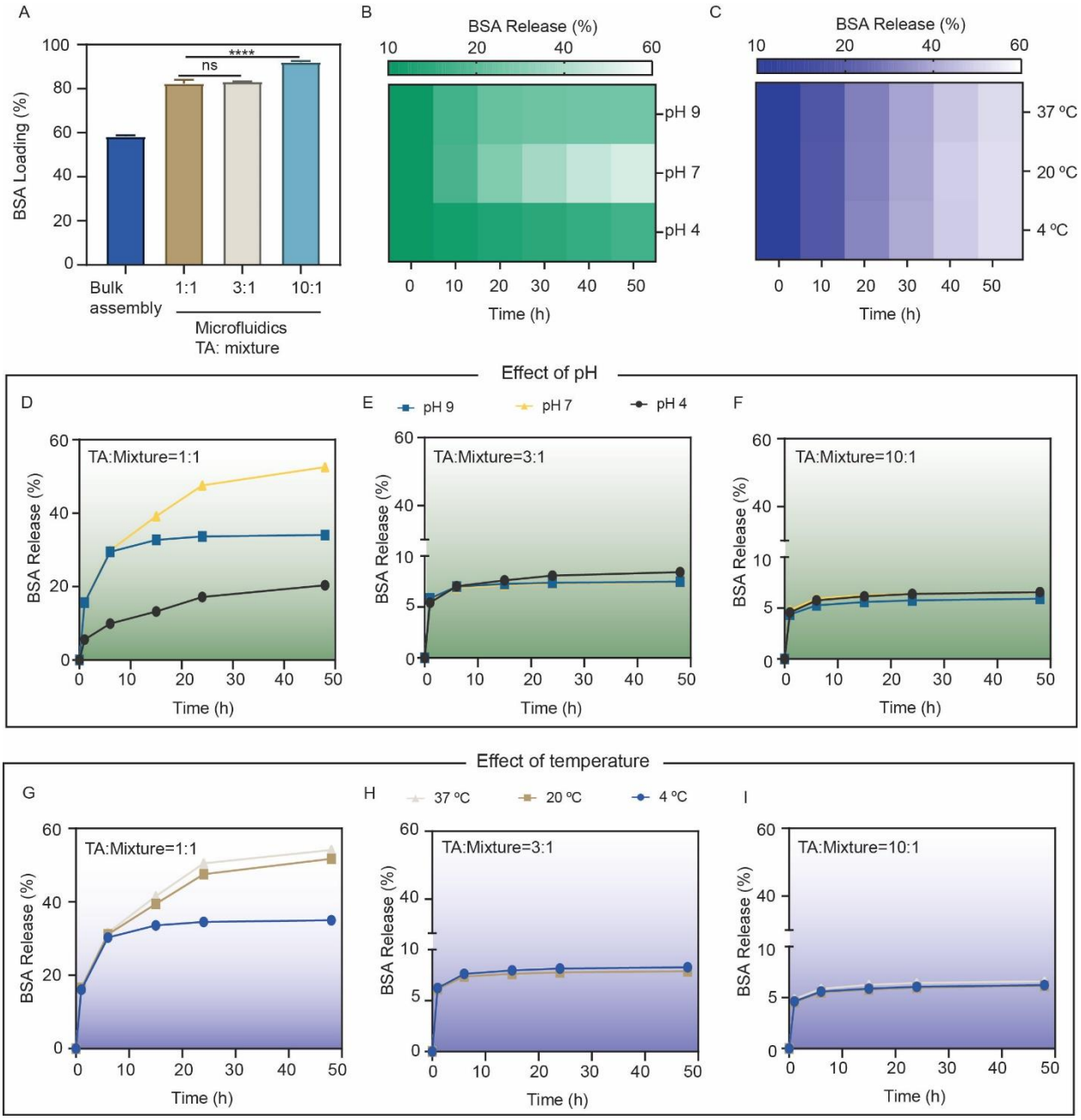

Figure 3. Loading and cumulative release of BSA from BSA-MPN NPs. (A) Loading of BSA in b-MPN NPs prepared via bulk assembly or microfluidics using different flow rate ratios (TA:mixture). Effect of (B) pH and (C) temperature on the release of BSA from bulk-assembled BSA-MPN NPs. Effects of (D–F) pH and (G–I) on the release of BSA from BSA-MPN NPs prepared via microfluidics using TA-to-mixture flow rate ratios of 1:1, 3:1, and 10:1. Three specimens were analyzed for each sample and data are shown as the mean ± SD. ns, not

significantly different; ****, $p < 0.0001$ with 95% confidence level from one-way analysis of variance.

Loading and Release Kinetics of Proteins. As the flow rate ratio is the microfluidic parameter that leads to the most significant difference in NP morphology, its effects on the ratio of TA to other precursors may also impact the loading and release profiles of the incorporated cargo. Hence, we explored the influence of flow rate ratio on the loading and release of BSA (a model cargo) from the microfluidics-assembled and bulk-assembled BSA-MPN NPs. As shown in Figure 3A, employing TA:mixture flow rate ratios of 1:1 and 3:1 resulted in a comparable loading of ~80%, which was improved to ~90% after increasing the flow rate ratio to 10:1. Furthermore, the BSA-MPN NPs prepared via microfluidics showed a higher BSA loading than the bulk-assembled NPs (~57%; the ratio of TA and other precursors used in bulk assembly is same as the flow rate ratio of 1:1 using in microfluidics assembly). This higher loading is likely due to the predominant flow regime in microfluidics being laminar, which may enable enhanced fine mixing of protein with other NP precursors, unlike the turbulent flow in bulk assembly.

We then investigated the BSA release profiles at different pH and temperatures. For bulk-assembled BSA-MPN NPs, only ~20% of BSA was released from the NPs after 48 h at pH 4, likely due to the strong interaction between BSA and polyphenols (e.g., hydrogen bonding).[33] Upon increasing the pH, a higher amount of BSA was released with a faster profile obtained at pH 7 (~50% within 48 h) than at pH 9 (~25% within 48 h) (Figures 3B and S21A). This is attributed to the combined influence of hydrogen bonding and metal coordination. The extent and strength of hydrogen bonding can be readily diminished at nonacidic pH, whereas metal coordination tends to be more stable at more alkaline pH, thereby rationalizing the more rapid release profile observed at pH 7 relative to those at pHs 4 and 9. In contrast, the release profiles of BSA from the NPs were comparable across the temperature range examined (Figures 3C

and S21B). For BSA-MPN NPs prepared via microfluidics, those assembled at a flow rate ratio of 1:1 (TA: mixture) displayed comparable BSA release profiles to those of the bulk-assembled BSA-MPN NPs obtained upon varying pH. In contrast, the BSA release behaviors of NPs prepared at flow rate ratios of 3:1 and 10:1 did not show any pH responsiveness and only <10% BSA was released after 48 h (Figure 3D–F). Compared to using a flow rate ratio of 1:1, using higher flow rate ratios i.e., 3:1 and 10:1 increased the proportion of TA, which likely resulted in enhanced binding with BSA and thus impeded the release of BSA from the MPN NPs.

Compared to the nondependent temperature response observed for the release of BSA from the bulk-assembled BSA-MPN NPs, temperature exhibited a more significant impact on BSA release from NPs prepared via microfluidics at a flow rate ratio of 1:1. More specifically, the release of BSA plateaued after 10 h and remained at 30% when incubating at 4 °C (Figure 3G). However, more sustained releases were observed after incubating at 20 and 37 °C and >50% of BSA was released after 48 h (Figure 3G). Similar to the negligible pH responsiveness observed, temperature minimally influenced the release of BSA from NPs prepared at the higher flow rate ratios of 3:1 and 10:1; <10% BSA was released after 48 h (Figure 3H, I).

We then investigated whether proteins were released in free form or as complexes via SDS-PAGE analysis. Both the gel bands of BSA released from the bulk-assembled BSA-MPN NPs and free BSA were observed at a comparable position (Figure S22), indicating that BSA was primarily released in free form from the bulk-assembled NPs. In contrast, the gel band of BSA released from the microfluidics-assembled BSA-MPN NPs shifted up (Figure S22), suggesting a higher molecular weight of the released component, which was likely due to the released BSA being complexed with other constituents of BSA-MPN NPs (e.g., polyphenols).

Cell Association of BSA_{FITC}-MPN NPs. The impact of flow rate ratio on the ratio of TA to other precursors significantly influenced the NP morphology and physicochemical properties. Therefore, it was also likely to affect NP–cell association. As the BSA-MPN NPs reported

herein (both bulk-assembled and microfluidics-assembled) demonstrated negligible cytotoxicity up to a particle-to-cell ratio of 4×10^6:1 (Figure S23), we investigated the influence of flow rate ratio on NP–cell interactions via cell association assays at a particle-to-cell ratio of 5×10^5:1. To improve reproducibility, reporting, and reanalysis, this study conforms to the MIRIBEL standard,[26] and a companion checklist is provided in the Supporting Information. As observed from Figure S24, following incubation for 4 h, <15% of cells were associated with BSA_{FITC}-MPN NPs prepared by microfluidics. Cell association was particularly negligible with NPs prepared at flow rate ratios of 3:1 and 10:1 (<3 %). The relative mean fluorescence intensity (R-MFI) decreased (from 2.1 to 0.9), and a left shift of the FITC histogram was observed when increasing the flow rate ratio (from 1:1 to 10:1) (Figure 4A, B), further supporting the observation that fewer NPs associated with cells. NPs became more negatively charged after increasing the flow rate ratio (Figure S8), which might impede their association with negatively charged cell membranes. In contrast, the bulk-assembled BSA_{FITC}-MPN NPs exhibited slightly higher cell association (~34 %) and R-MFI (3.6) (Figure 4A, B and Figure S24). At 24 h, the cell association and R-MFI of the bulk-assembled BSA_{FITC}-MPN NPs further increased to 55% and 6.5, respectively, whereas the cell association and R-MFI of the BSA_{FITC}-MPN NPs assembled via microfluidics at flow rate ratios of 1:1 and 10:1 remained at low levels (19% and 2%, and 2.7 and 1.5, respectively; Figure 4A, C and Figure S24). However, the BSA_{FITC}-MPN NPs prepared at a flow ratio of 3:1 demonstrated significantly higher cell association (55%) and R-MFI (4.0) after 24 h (Figure 4A, C and Figure S24), likely due to their larger size (Figure 2B), which plays a more dominant role for cell association for a long period of incubation. Confocal laser scanning microscopy (CLSM) was then used to qualitatively analyze the interaction of NPs with cells. As shown in Figure 4D, both types of assembly strategy resulted in particles that could be internalized by cells. To investigate the mechanism of cell internalization, we further conducted a colocalization study of NPs with lysosomes. The

partial overlap of green (i.e., the signal from NPs) and red fluorescence (i.e., the signal from lysosomes) indicates the colocalization of NPs and lysosomes (Figure S25), suggesting that NPs were internalized via endocytosis and might go through the endo/lysosomal pathway.

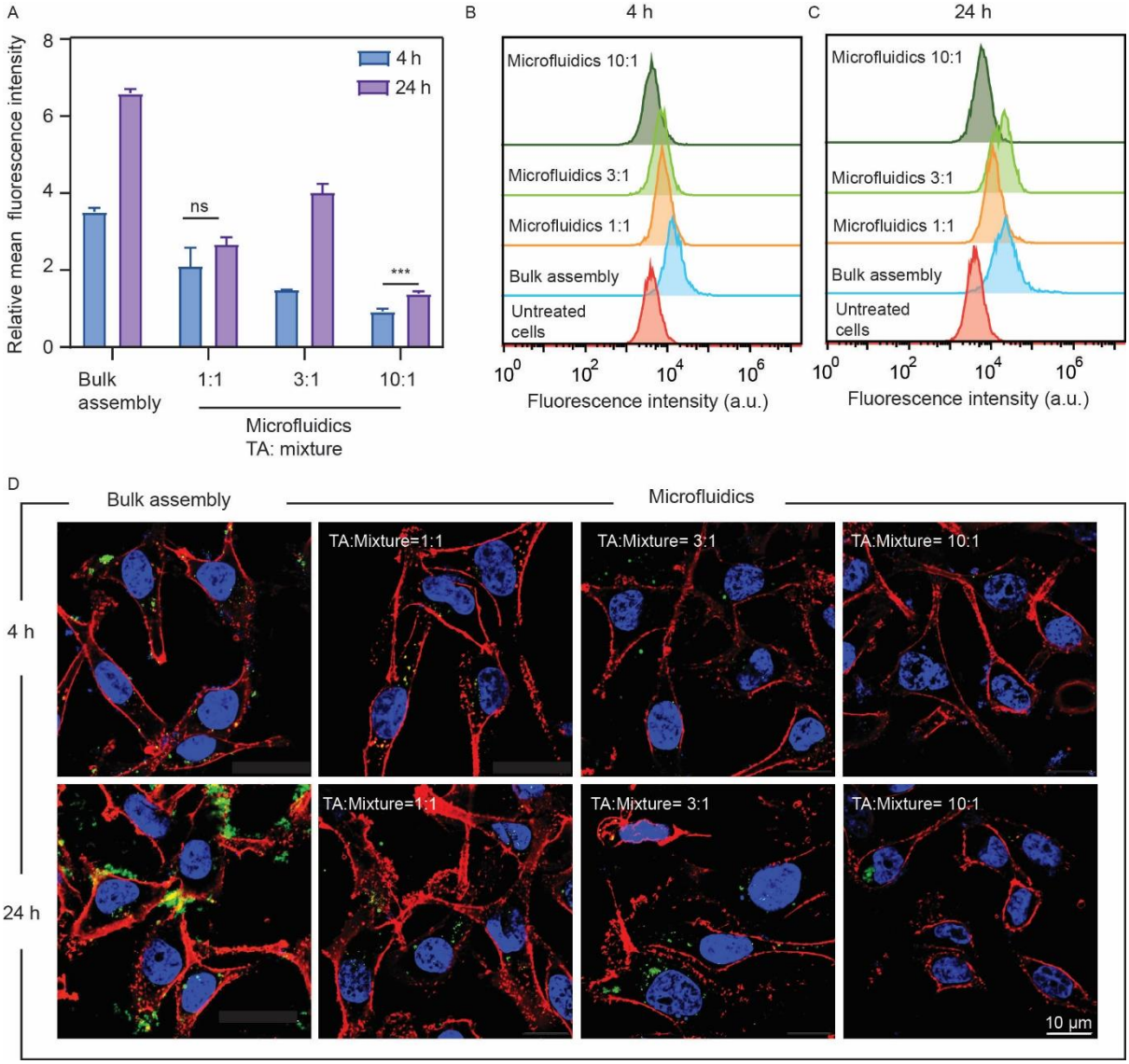

Figure 4. (A) Cell association of BSA_{FITC}-MPN NPs, as assessed from relative mean fluorescence intensity measurements (relative to untreated cells) and (B,C) corresponding FITC histograms of MDA-MB-231 cells treated with BSA_{FITC}-MPN NPs prepared via bulk assembly and microfluidics (using different TA:mixture flow rate ratios) for 4 and 24 h at 37 °C. FITC-BSA was used for NP assembly to endow fluorescence to the resultant NPs. "ns" denotes not significantly different with 95% confidence level from unpaired *t*-test; ***, $p < 0.001$ with 95% confidence level from unpaired *t*-test. (D) CLSM images of MDA-MB-231

cells treated with BSA_{FITC}-MPN NPs prepared via bulk assembly and microfluidics (using different TA:mixture flow rate ratio) for 4 and 24 h at 37 °C. NPs (green) were labeled via incorporating FITC-labelled BSA (BSA_{FITC}). Cell membranes (red) and nuclei (blue) were stained with WGA594 and Hoechst 33342, respectively.

Versatility of NP Assembly Via Microfluidics. To demonstrate the versatility of NP assembly via microfluidics, the size range of the b-MPN NPs prepared using microfluidics was compared with that obtained for analogous NPs that were prepared via bulk assembly, as reported recently.[23] As shown in Figure 5A, the bulk-assembled b-MPN NPs displayed a size range of ~45–220 nm, whereas the microfluidics-assembled b-MPN NPs displayed a broader size range of ~37–330 nm, highlighting the potential of further tailoring size profiles via microfluidics. In addition, the microfluidics-mediated NP assembly enabled the preparation of NPs without bioactive cargo or with diverse proteins with specific aliphatic indexes (AIs), M_w, and isoelectric point (PI), including PEP (AI = 91.38, PI = 3.2, M_w = 34.5 kDa), GOx (AI = 86.12, PI = 4.2, M_w = 160 kDa), and LYZ (AI = 82.93, PI = 10.8, M_w = 14 kDa). The NPs prepared without bioactive cargo were similar in size to BSA-MPN NPs (Figure 5B, C, Figure S26, Table S7). Incorporating proteins with a higher AI generally produced larger NPs (Figure 5B, C, Figure S26, Table S7), as proteins with a higher AI generally contain more aliphatic and hydrophobic chains that can have stronger hydrophobic interactions with TA.[33] However, the GOx-MPN NPs were smaller than the LYZ-MPN NPs though GOx displays a higher AI than LYZ. This finding might be attributed to the significantly higher PI of LYZ,[33] which also can contribute to ionic interactions with TA. No correlation between biomacromolecule PI/M_w and NP size was observed.

A summary of the key differences between b-MPN NPs prepared via bulk assembly and microfluidics is presented in Table S8. These differences include the mixing protocol, flow regime, NP size range, protein loading and release kinetics, and NP–cell interactions.

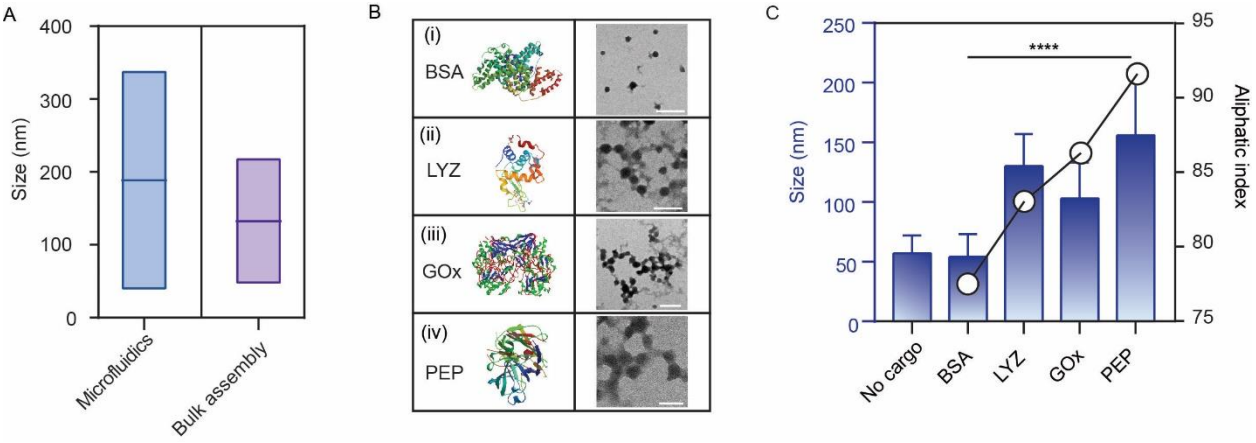

Figure 5. Versatility of b-MPN NP assembly via microfluidics. (A) Comparison of the size range obtained for the preparation of BSA-MPN NPs via microfluidics and bulk assembly. (B) TEM images and (C) size of MPN NPs without or with different types of proteins, as prepared by microfluidics; scale bars are 200 nm. Three specimens were analyzed for each sample, with the data shown as the mean ± SD, ****$p < 0.0001$.

CONCLUSION

In this study, we demonstrated the use of microfluidics to engineer MPN NPs by altering microfluidics operating (flow rate ratio, total flow rate, temperature) and NP composition (PEG M_w, Fe^{III} concentration, protein type) parameters. Among the microfluidic operating parameters examined, the flow rate ratio played a dominant role in influencing the particle size and morphology, the release kinetics of the incorporated proteins, and cell association. When comparing the effect of nanoparticle composition on NP size, increasing the M_w of PEG led to a size reduction of b-MPN NPs prepared via microfluidics, whereas a reverse trend was observed for the bulk-assembled MPN NPs. In contrast, increasing the concentration of Fe^{III} had a comparable effect on the size of the MPN NPs regardless of the assembly route. The microfluidics-assembled b-MPN NPs displayed a larger size range, when compared with the bulk-assembled NPs, and could incorporate a range of proteins with distinct AI. The NPs prepared via microfluidics showed a ~30% higher loading of BSA than those prepared via bulk assembly. BSA-MPN NPs prepared via microfluidics with a flow rate ratio of 1:1 displayed a

similar release profile to the bulk-assembled BSA-MPN NPs at 20 ℃ in response to varying pH but showed a slower release pattern at 4 ℃. However, the release profiles of BSA-MPN NPs prepared at flow rate ratios of 3:1 and 10:1 were unaffected by changes in pH or temperature and less than 10% of BSA was released after 48 h. When comparing NP–cell behaviors, the bulk-assembled b-MPN NPs displayed a higher degree of cell association than the microfluidics-assembled b-MPN NPs but NPs prepared via both assembly strategies could be internalized by cells after incubation for 24 h. These results highlight how microfluidics can be employed to engineer the physicochemical properties of NPs and adjust their degree of association with cells. The microfluidic device, NanoAssemblr Ignite, used in the present study features two inlets (for the injection of TA and mixture, respectively) and a Y-shaped microfluidic channel, and allows for the adjustment of three operating parameters (i.e., flow rate ratio, total flow rate, and temperature) for NP assembly. We envision that the use of microfluidic devices with multiple inlets and an optimized microfluidic channel geometry may allow a more thorough mixing of each precursor within an enhanced laminar flow regime, which may further improve control over the assembly of MPN NPs. Moreover, lengthening the channel after the junction points where the regents combine may prolong the mixing time and enable better stabilization of MPN NPs. We also note that microfluidics assembly readily allows scale up, including with commercial microfluidic devices comparable to the one used in the present study.[34–36] Designing a large microfluidic platform with multiple parallel microfluidic channels or multilayer microfluidic chips may allow larger-scale production of MPN NPs for future commercialization.

ASSOCIATED CONTENT

Supporting Information. Photographs of NanoAssemblr Ignite; BSA calibration curves, ζ-potentials, UV–vis spectroscopy, size, and PDI data, cell viability and cell association of

BSA-MPN-NPs; summary of differences between b-MPN NPs prepared via microfluidics and bulk assembly; and MIRIBEL checklist.

AUTHOR INFORMATION

Corresponding Author

*fcaruso@unimelb.edu.au

Author Contributions

‡J.C. and S.S. contributed equally to this work. The manuscript was written through contributions of all authors. All authors have given approval to the final version of the manuscript.

Notes

The authors declare no competing financial interest.

ACKNOWLEDGMENT

F.C. acknowledges the award of a National Health and Medical Research Council (NHMRC) Leadership Fellowship (GNT2016732). This work was performed in part at the Materials Characterisation and Fabrication Platform (MCFP) and Melbourne Advanced Microscopy Facility at The University of Melbourne, and the Victorian Node of the Australian National Fabrication Facility (ANFF). TEM analyses were conducted using the facilities at the Biosciences Microscopy Unit, School of Bioscience, The University of Melbourne. A.C.S and Y.A.B acknowledge funding from the European Union's Horizon 2020 research and innovation programme under grant agreement H2020-MSCA-RISE-778001 and the Basque Government under Grupos Consolidados (grant no. IT1633-22). The authors acknowledge Dr Christina Cortez-Jugo and Dr Zhixing Lin for helpful discussions, and Yuang Gu for assistance with the SDS-PAGE analysis.

REFERENCES

1. Zhang, S.; Tan, E.; Wang, R.; Gao, P.; Wang, H.; Cheng, Y. Robust Reversible Cross-Linking Strategy for Intracellular Protein Delivery with Excellent Serum Tolerance. *Nano Lett.* **2022**, *22*, 8233–8240.

2. Xu, C.; Wang, Y.; Yu, H.; Tian, H.; Chen, X. Multifunctional Theranostic Nanoparticles Derived from Fruit-Extracted Anthocyanins with Dynamic Disassembly and Elimination Abilities. *ACS Nano* **2018**, *12*, 8255–8265.

3. Li, J.; Liu, X.; Zhou, Z.; Tan, L.; Wang, X.; Zheng, Y.; Han, Y.; Chen, D. F.; Yeung, K. W. K.; Cui, Z.; Yang, X.; Liang, Y.; Li, Z.; Zhu, S.; Wu, S. Lysozyme-Assisted Photothermal Eradication of Methicillin-Resistant *Staphylococcus aureus* Infection and Accelerated Tissue Repair with Natural Melanosome Nanostructures. *ACS Nano* **2019**, *13*, 11153–11167

4. Yuan, C.; Levin, A.; Chen, W.; Xing, R.; Zou, Q.; Herling, T. W.; Challa, P. K.; Knowles, T. P. J.; Yan, X. Nucleation and Growth of Amino Acid and Peptide Supramolecular Polymers through Liquid–Liquid Phase Separation. *Angew. Chem. Int. Ed.* **2019**, *58*, 18116–18123.

5. Ge, F.; Wei, S.; Liu, Z.; Wang, G.; Wang, X.; Zhang, G.; Lu, H.; Cho, K.; Qiu, L. Tailoring Structure and Field-Effect Characteristics of Ultrathin Conjugated Polymer Films via Phase Separation. *ACS Appl. Mater. Interfaces* **2018**, *10*, 9602–9611.

6. Yao, M. S.; Lv, X. J.; Fu, Z. H.; Li, W. H.; Deng, W. H.; Wu, G. D.; Xu, G. Layer-by-Layer Assembled Conductive Metal–Organic Framework Nanofilms for Room-Temperature Chemiresistive Sensing. *Angew. Chem. Int. Ed.* **2017**, *56*, 16510–16514.

7. Zhong, Q. Z.; Pan, S.; Rahim, M. A.; Yun, G.; Li, J.; Ju, Y.; Lin, Z.; Han, Y.; Ma, Y.; Richardson, J. J.; Caruso, F. Spray Assembly of Metal–Phenolic Networks: Formation, Growth, and Applications. *ACS Appl. Mater. Interfaces* **2018**, *10*, 33721–33729.

8. Troyano, J.; Camur, C.; Garzon-Tovar, L.; Carne-Sanchez, A.; Imaz, I.; Maspoch, D. Spray-Drying Synthesis of MOFs, COFs, and Related Composites. *Acc. Chem. Res.* **2020**, *53*, 1206–1217.

9. Bhangu, S. K.; Fernandes, S.; Beretta, G. L.; Tinelli, S.; Cassani, M.; Radziwon, A.; Wojnilowicz, M.; Sarpaki, S.; Pilatis, I.; Zaffaroni, N.; Forte, G.; Caruso, F.; Ashokkumar, M.; Cavalieri, F. Transforming the Chemical Structure and Bio-Nano Activity of Doxorubicin by Ultrasound for Selective Killing of Cancer Cells. *Adv. Mater.* **2022**, *34*, 2107964.

10. Athinarayanan, J.; Periasamy, V. S.; Alshatwi, A. A. Fabrication of Cellulose Nanocrystal-Decorated Hydroxyapatite Nanostructures Using Ultrasonication for Biomedical Applications. *Biomass Convers. Biorefin.* **2021**, *13*, 5861–5874.

11. Balasubramaniam, M.; Balakumar, S. Nanostructuring of Silver Nanoparticles Anchored 1D Zinc Antimonate Electrode Material by Ultrasonication Assisted Chemical Reduction Approach for Supercapacitors. *Mater. Chem. Phys.* **2019**, *224*, 334–348.

12. Xue, L.; Gong, N.; Shepherd, S. J.; Xiong, X.; Liao, X.; Han, X.; Zhao, G.; Song, C.; Huang, X.; Zhang, H.; Padilla, M. S.; Qin, J.; Shi, Y.; Alameh, M. G.; Pochan, D. J.; Wang, K.; Long, F.; Weissman, D.; Mitchell, M. J. Rational Design of Bisphosphonate Lipid-like Materials for mRNA Delivery to the Bone Microenvironment. *J. Am. Chem. Soc.* **2022**, *144*, 9926–9937.

13. Wang, W.; Zhang, M. J.; Chu, L. Y. Functional Polymeric Microparticles Engineered from Controllable Microfluidic Emulsions. *Acc. Chem. Res.* **2014**, *47*, 373–384.

14. Kim, J.; Jozic, A.; Lin, Y.; Eygeris, Y.; Bloom, E.; Tan, X.; Acosta, C.; MacDonald, K. D.; Welsher, K. D.; Sahay, G. Engineering Lipid Nanoparticles for Enhanced Intracellular Delivery of mRNA through Inhalation. *ACS Nano* **2022**, *16*, 14792–14806.

15. Ye, Z.; Wang, K.; Lou, M.; Jia, X.; Xu, F.; Ye, G. Consecutive Synthesis of Gold Nanobipyramids with Controllable Morphologies Using a Microfluidic Platform. *Microfluid. Nanofluid.* **2020**, *24*, 38.

16. Chen, X.; Lv, H. Intelligent Control of Nanoparticle Synthesis on Microfluidic Chips with Machine Learning. *NPG Asia Mater.* **2022**, *14*, 69.

17. Li, P.; Wang, C.; Qiu, J.; Song, F.; Huang, Y.; Zhang, Y.; Zhang, K.; Ji, H.; Sang, Y.; Blaker, J. J.; Zhang, Y.; Han, L. Inhibitory Effect of Zinc Oxide Nanorod Arrays on Breast Cancer Cells Profiled through Real-Time Cytokines Screening by a Single-Cell Microfluidic Platform. *BMEMat* **2023**, e12040. DOI: 10.1002/bmm2.12040

18. Wang, C.; Wang, S.; Kang, D. D.; Dong, Y. Biomaterials for In Situ Cell Therapy. *BMEMat* **2023**, e12037. DOI: 10.1002/bmm2.12039

19. Liu, Z.; Fontana, F.; Python, A.; Hirvonen, J. T.; Santos, H. A. Microfluidics for Production of Particles: Mechanism, Methodology, and Applications. *Small* **2019**, *16*, 1904673.

20. Zhu, P.; Wang, L. Microfluidics-Enabled Soft Manufacture of Materials with Tailorable Wettability. *Chem. Rev.* **2022**, *122*, 7010–7060.

21. Liu, Y.; Sun, L.; Zhang, H.; Shang, L.; Zhao, Y. Microfluidics for Drug Development: From Synthesis to Evaluation. *Chem. Rev.* **2021**, *121*, 7468–7529.

22. Hu, C.; Bai, Y.; Hou, M.; Wang, Y.; Wang, L.; Cao, X.; Chan, C. W.; Sun, H.; Li, W.; Ge, J.; Ren, K. Defect-Induced Activity Enhancement of Enzyme-Encapsulated Metal–Organic Frameworks Revealed in Microfluidic Gradient Mixing Synthesis. *Sci. Adv.* **2020**, *6*, eaax5785.

23. Chen, J.; Pan, S.; Zhou, J.; Lin, Z.; Qu, Y.; Glab, A.; Han, Y.; Richardson, J. J.; Caruso, F. Assembly of Bioactive Nanoparticles via Metal–Phenolic Complexation. *Adv. Mater.* **2022**, *34*, 210624.

24. Tian, W.; VahidMohammadi, A.; Wang, Z.; Ouyang, L.; Beidaghi, M.; Hamedi, M. M. Layer-by-Layer Self-Assembly of Pillared Two-Dimensional Multilayers. *Nat. Commun.* **2019**, *10*, 2558.

25. Guo, J.; Tardy, B. L.; Christofferson, A. J.; Dai, Y.; Richardson, J. J.; Zhu, W.; Hu, M.; Ju, Y.; Cui, J.; Dagastine, R. R.; Yarovsky, I.; Caruso, F. Modular Assembly of Superstructures from Polyphenol-Functionalized Building Blocks. *Nat. Nanotechnol.* **2016**, *11*, 1105–1111.

26. Faria, M.; Bjornmalm, M.; Thurecht, K. J.; Kent, S. J.; Parton, R. G.; Kavallaris, M.; Johnston, A. P. R.; Gooding, J. J.; Corrie, S. R.; Boyd, B. J.; Thordarson, P.; Whittaker, A. K.; Stevens, M. M.; Prestidge, C. A.; Porter, C. J. H.; Parak, W. J.; Davis, T. P.; Crampin, E. J.; Caruso, F. Minimum Information Reporting in Bio–Nano Experimental Literature. *Nat. Nanotechnol.* **2018**, *13*, 777–785.

27. Ejima, H.; Richardson, J. J.; Liang, K.; Best, J. P.; Koeverden, M.; Such, G. K.; Cui, J.; Caruso, F. One-Step Assembly of Coordination Complexes for Versatile Film and Particle Engineering. *Science* **2013**, *341*, 154–157.

28. Bhangu, S. K.; Charchar, P.; Noble, B. B.; Kim, C. J.; Pan, S.; Yarovsky, I.; Cavalieri, F.; Caruso, F. Origins of Structural Elasticity in Metal–Phenolic Networks Probed by Super-Resolution Microscopy and Multiscale Simulations. *ACS Nano* **2021**, *16*, 98–110.

29. Amirilargani, M.; Sabetghadam, A.; Mohammadi, T. Polyethersulfone/Polyacrylonitrile Blend Ultrafiltration Membranes with Different Molecular Weight of Polyethylene Glycol: Preparation, Morphology and Antifouling Properties. *Polym. Adv. Technol.* **2012**, *23*, 398–407.

30. Jenkins, C. L.; Meredith, H. J.; Wilker, J. J. Molecular Weight Effects Upon the Adhesive Bonding of a Mussel Mimetic Polymer. *ACS Appl. Mater. Interfaces* **2013**, *5*, 5091−5096.

31. Mazaheri, O.; Alivand, M. S.; Zavabeti, A.; Spoljaric, S.; Pan, S.; Chen, D.; Caruso, F.; Suter, H. C.; Mumford, K. A. Assembly of Metal–Phenolic Networks on Water-Soluble Substrates in Nonaqueous Media. *Adv. Funct. Mater.* **2022**, *32*, 2111942.

32. Rahim, M. A.; Björnmalm, M.; Bertleff-Zieschang, N.; Besford, Q.; Mettu, S.; Suma, T.; Faria, M.; Caruso, F. Rust-Mediated Continuous Assembly of Metal–Phenolic Networks. *Adv. Mater.* **2017**, *29*, 1606717.

33. Han, Y.; Lin, Z.; Zhou, J.; Yun, G.; Guo, R.; Richardson, J. J.; Caruso, F. Polyphenol-Mediated Assembly of Proteins for Engineering Functional Materials. *Angew. Chem. Int. Ed.* **2020**, *59*, 15618–15625.

34. Cui, L.; Pereira, S.; Sonzini, S.; van Pelt, S.; Romanelli, S. M.; Liang, L.; Ulkoski, D.; Krishnamurthy, V. R.; Brannigan, E.; Brankin, C.; Desai, A. S. Development of a High-Throughput Platform for Screening Lipid Nanoparticles for mRNA Delivery. *Nanoscale* **2022**, *14*, 1480–1491.

35. Wang, X.; Liu, S.; Sun, Y.; Yu, X.; Lee, S. M.; Cheng, Q.; Wei, T.; Gong, J.; Robinson, J.; Zhang, D.; Lian, X.; Basak, P.; Siegwart, D. J. Preparation of Selective Organ-Targeting (SORT) Lipid Nanoparticles (LNPs) Using Multiple Technical Methods for Tissue-Specific mRNA Delivery. *Nat. Protoc.* **2023**, *18*, 265–291.

36. Webb, C.; Forbes, N.; Roces, C. B.; Anderluzzi, G.; Lou, G.; Abraham, S.; Ingalls, L.; Marshall, K.; Leaver, T. J.; Watts, J. A.; Aylott, J. W.; Perrie, Y. Using Microfluidics for Scalable Manufacturing of Nanomedicines from Bench to GMP: A Case Study Using Protein-Loaded Liposomes. *Int. J. Pharm.* **2020**, *582*, 119266.

Table of contents graphic